Schwarzschild and Ledoux are equivalent on evolutionary timescales

Evan H. Anders,[1,2] Adam S. Jermyn,[3,2] Daniel Lecoanet,[1,4,5] Adrian E. Fraser,[6,2] Imogen G. Cresswell,[7,2] and J. R. Fuentes[8]

[1]CIERA, Northwestern University, Evanston IL 60201, USA
[2]Kavli Institute for Theoretical Physics, University of California, Santa Barbara, CA 93106, USA
[3]Center for Computational Astrophysics, Flatiron Institute, New York, NY 10010, USA
[4]Department of Engineering Sciences and Applied Mathematics, Northwestern University, Evanston IL 60208, USA
[5]Kavli Institute for Theoretical Physics, University of California, Santa Barbara, Santa Barbara, CA 93106, USA
[6]Department of Applied Mathematics, Baskin School of Engineering, University of California, Santa Cruz, Santa Cruz, CA 95064, USA
[7]Department Astrophysical and Planetary Sciences & LASP, University of Colorado, Boulder, CO 80309, USA
[8]Department of Physics and McGill Space Institute, McGill University, 3600 rue University, Montreal, QC H3A 2T8, Canada

ABSTRACT

In one-dimensional stellar evolution models, convective boundaries are calculated using either the Schwarzschild or Ledoux criterion, but there is no consensus regarding which criterion to use. In this letter, we present a 3D hydrodynamical simulation of a convection zone whose boundary is thermally unstable but compositionally stable. Therefore, the convective boundary is Schwarzschild unstable but Ledoux stable. Over many convective overturn timescales, entrainment makes the convection zone grow. The convective boundary stops advancing after it becomes stable by the Schwarzschild criterion. This work demonstrates using 3D simulations that the Ledoux criterion *instantaneously* describes the boundary of a convection zone, but that Ledoux-stable boundaries are fragile unless they are also Schwarzschild stable. Therefore, the Schwarzschild stability criterion describes the size of a convection zone, except during short-lived evolutionary stages in which entrainment persists.

1. INTRODUCTION

Observations tell us that we do not understand the positioning of convective boundaries in stars. For example, models and observations disagree about the sizes of convective cores (Claret & Torres 2018; Viani & Basu 2020; Pedersen et al. 2021; Johnston 2021), lithium abundances in solar-type stars (Pinsonneault 1997; Sestito & Randich 2005; Carlos et al. 2019; Dumont et al. 2021), and the sound speed at the base of the Sun's convection zone (see Basu 2016, Sec. 7.2.1). Improperly estimating convective boundary locations can have important impacts across astrophysics such as by affecting the mass of stellar remnants (Farmer et al. 2019; Mehta et al. 2022)

and the inferred radii of exoplanets (Basu et al. 2012; Morrell 2020).

While convective boundary mixing (CBM) has many uncertainties, the most fundamental question is: what determines the location of convection zone boundaries? Some authors evaluate the *Schwarzschild criterion*, which determines where the temperature and pressure stratification within a star are stable or unstable. Others evaluate the *Ledoux criterion*, which accounts for stability or instability due to compositional stratification (e.g., the variation of helium abundance with pressure; see Salaris & Cassisi 2017, chapter 3, which reviews these criteria). Recent authors state that these criteria should be equivalent at a convective boundary according to mixing length theory (Gabriel et al. 2014; Paxton et al. 2018, 2019), but in practice these criteria are often different at convective boundaries in stellar evolu-

Corresponding author: Evan H. Anders
evan.anders@northwestern.edu

tion software instruments, and a variety of workarounds have been proposed to address this (Paxton et al. 2018, 2019).

There is still disagreement regarding which stability criterion to employ (discussed in Kaiser et al. 2020, chapter 2). Multi-dimensional simulations show that convection zones with Ledoux-stable boundaries expand by entraining compositionally-stable regions (Meakin & Arnett 2007; Woodward et al. 2015; Jones et al. 2017; Cristini et al. 2019; Fuentes & Cumming 2020; Andrassy et al. 2020, 2021). It is unclear from past 3D simulations whether that entrainment should stop, leading to uncertainty in how to include entrainment in 1D models (Staritsin 2013; Scott et al. 2021).

In this letter, we present a simple 3D hydrodynamical simulation that demonstrates that convection zones with Ledoux-stable but Schwarzschild-unstable boundaries entrain material until the Ledoux and Schwarzschild criteria agree on the location of the convective boundary. Therefore, in 1D stellar evolution models, when evolutionary timescales are much larger than the convective overturn timescale (such as on the main sequence, see Georgy et al. 2021), the Schwarzschild criterion describes the location of the convective boundary, and Ledoux and Schwarzschild should agree if properly implemented. We discuss these criteria in Sec. 2, display simulations in Sec. 3, and briefly discuss in Sec. 4.

2. THEORY & EXPERIMENT

Convective stability can be determined using the Schwarzschild criterion,

$$\mathcal{Y}_{\mathrm{S}} \equiv \nabla_{\mathrm{rad}} - \nabla_{\mathrm{ad}}, \tag{1}$$

or the Ledoux criterion,

$$\mathcal{Y}_{\mathrm{L}} \equiv \mathcal{Y}_{\mathrm{S}} + \frac{\chi_\mu}{\chi_T}\nabla_\mu. \tag{2}$$

The temperature gradient $\nabla \equiv d\ln P/d\ln T$ (pressure P and temperature T) is ∇_{ad} for an adiabatic stratification and ∇_{rad} if the flux is entirely carried radiatively. The composition gradient $\nabla_\mu = d\ln\mu/d\ln P$ (mean molecular weight μ) is modified by $\chi_T = (d\ln P/d\ln T)_{\rho,\mu}$ and $\chi_\mu = (d\ln P/d\ln\mu)_{\rho,T}$ (density ρ).

In Eqns. 1 and 2, $\mathcal{Y}$ is the discriminant (e.g., Paxton et al. 2018, sec. 2), which is like the superadiabaticity. Stellar structure software instruments assume that convective boundaries coincide with the root (sign change) of the discriminant. The various stability regimes which can occur in stars are described in section 3 and figure 3 of Salaris & Cassisi (2017), but note four important regimes:

1. Convection Zones (CZs): Regions with $\mathcal{Y}_{\mathrm{S}} > 0$ and $\mathcal{Y}_{\mathrm{L}} \geq \mathcal{Y}_{\mathrm{S}}$ are convectively unstable.

2. Radiative Zones (RZs): Regions with $\mathcal{Y}_{\mathrm{S}} < 0$ and $\mathcal{Y}_{\mathrm{L}} \leq \mathcal{Y}_{\mathrm{S}}$ are stable to convection.

3. "Semiconvection" Zones (SZs): Regions with $\mathcal{Y}_{\mathrm{S}} > 0$ but $\mathcal{Y}_{\mathrm{L}} < 0$ are stablized to convection by a composition gradient despite an unstable thermal stratification. These regions can be stable RZs or linearly unstable to oscillatory doubly diffusive convection (ODDC, see Garaud 2018, chapters 2 and 4).

4. "Thermohaline" Zones: Regions with $\mathcal{Y}_{\mathrm{S}} < 0$ and $\mathcal{Y}_{\mathrm{L}} > \mathcal{Y}_{\mathrm{S}}$ are thermally stable to convection despite an unstable composition gradient. These regions can be stable RZs or linearly unstable to thermohaline mixing (see Garaud 2018, chapters 2 and 3).

In this paper, we study 3D simulations of a stable SZ (#3) bounded below by a CZ (#1) and above by an RZ (#2). We examine how the boundary of the CZ evolves through entrainment. In particular, we are interested in seeing if the roots of $\mathcal{Y}_{\mathrm{S}}$ and $\mathcal{Y}_{\mathrm{L}}$ coincide after evolution.

In this work, we utilize a simplified 3D model employing the Boussinesq approximation, which assumes that the depth of the layer being studied is much smaller than the local scale height. Since we are studying thin regions near convective boundaries, this assumption is okay. The relevant physics for this problem are included (∇_{rad} varies with height, buoyancy is determined both by the composition μ and the temperature stratification T), so $\mathcal{Y}_{\mathrm{S}}$ and $\mathcal{Y}_{\mathrm{L}}$ are meaningfuly defined and distinct from one another when composition gradients are present. For details on our model setup and Dedalus simulations, we refer the reader to appendices A and B.

3. RESULTS

Fig. 1 visualizes the composition field in our simulation near the initial state (left) and evolved state (right). Overplotted horizontal lines correspond to the roots of $\mathcal{Y}_{\mathrm{L}}$ (orange, Ledoux boundary) and $\mathcal{Y}_{\mathrm{S}}$ (purple, Schwarzschild boundary). Initially, the bottom third of the domain is a CZ, the middle third is an SZ, and the top third is an RZ. Convection mechanically overshoots at all times, which can be seen by the presence of convection slightly above the orange Ledoux boundary. Overshoot occurs because the Ledoux boundary corresponds to the sign change in the buoyant acceleration, not where the convective velocity is zero.

The most obvious change from the left to the right panel is that the CZ has consumed the SZ and fills the bottom two-thirds of the box. The overshooting convective motions entrained low-composition material
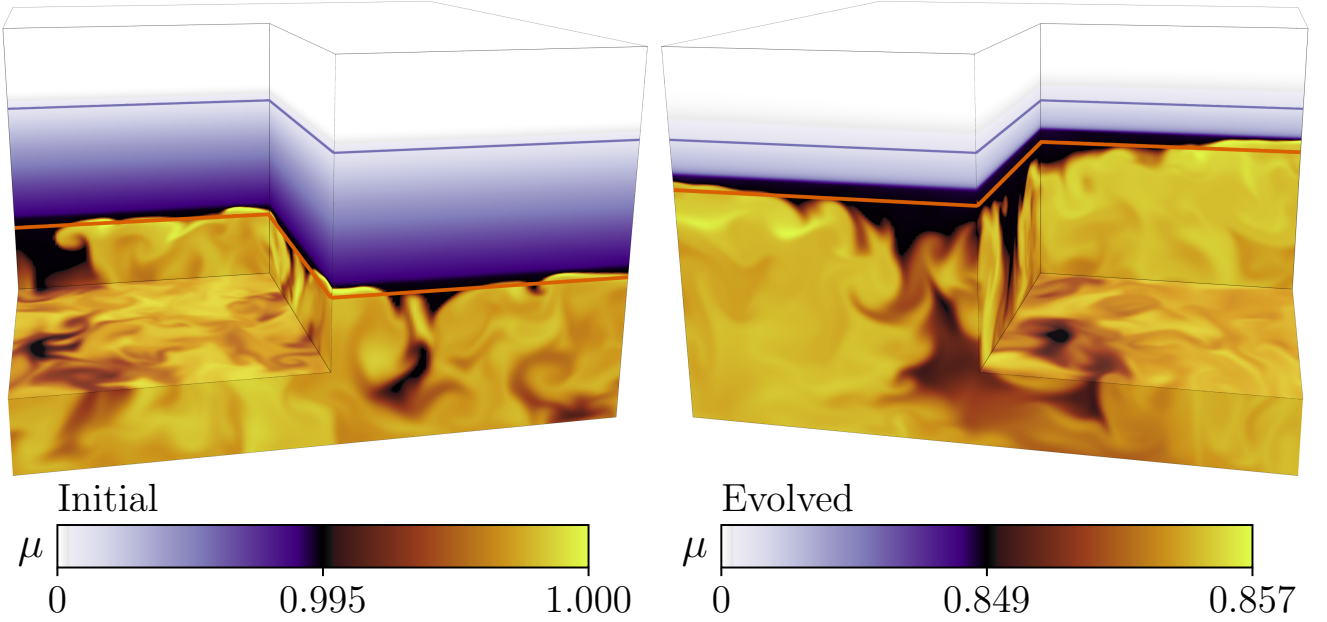
Figure 1. Volume renderings of the simulation composition field μ at early (left) and late (right) times. The change in color from white at the top of the box to dark purple at the top of the convection zone denotes a stable composition gradient. The convection zone is mostly well-mixed, so we expand the colorbar scaling there; black represents entrained low-μ fluid being mixed into the yellow high-μ convection zone. The orange and purple horizontal lines respectively denote the Ledoux and Schwarzschild boundaries. The simulation domain spans $z = [0,3]$, but we only plot $z = [0, 2.5]$ here. Note: this is currently evolving further.

from above the Ledoux boundary into the CZ. Convective motions mixed this fluid, and this process repeated over thousands of convective overturn times until the Ledoux and Schwarzschild boundaries of the CZ coincided. After becoming Schwarzschild stable, the convective boundary stopped moving. This occurs because the radiative flux renews and reinforces the radiative gradient, but there is no equivalent process for the composition.

Figure 2 displays vertical simulation profiles in the initial (left) and evolved (right) states. Shown are the composition μ (top), the discriminants $\mathcal{Y}_\mathrm{L}$ and $\mathcal{Y}_\mathrm{S}$ (middle), and the square Brunt-Väisälä frequency (top) as well as the square convective frequency defined as

$$f_{\mathrm{conv}}^2 = \frac{|\boldsymbol{u}|^2}{\ell_{\mathrm{conv}}^2}, \tag{3}$$

where $\boldsymbol{u}$ is the velocity and ℓ_{conv} is the depth of the convectively unstable layer.

Initially, the composition is uniform in the CZ ($z < 1$) and RZ ($z > 2$), but varies linearly in the SZ ($z \in [1,2]$). The root of $\mathcal{Y}_\mathrm{L}$ occurs at $z \approx 1$ while that of $\mathcal{Y}_\mathrm{S}$ occurs at $z \approx 2$. Furthermore, $f_{\mathrm{conv}}^2 = 0$ in the initial, stationary state. The Brunt-Väisälä frequency N^2 is negative in a boundary layer at the base of the CZ which drives the

instability. N^2 is stable for $z \gtrsim 1$, and is larger in the RZ than the SZ by an order of magnitude[1]

The evolved state is attained after convection entrains and mixes the stabilizing fluid in the SZ. We see that the composition profile (top) is constant in the CZ and overshoot zone (denoted as a transparent hashed region), but approximates a step function at the top of the overshoot zone. The roots of the discriminants $\mathcal{Y}_\mathrm{L}$ and $\mathcal{Y}_\mathrm{S}$ coincide (middle). Furthermore, in the CZ, the convective frequency is roughly constant and $N^2 \lesssim 0$ (bottom). In the RZ, $f_{\mathrm{conv}}^2 \approx 0$ and $N^2 \gg 0$. We can compute the "stiffness" of the radiative-convective interface,

$$\mathcal{S} = \frac{N^2|_{\mathrm{RZ}}}{f_{\mathrm{conv}}^2|_{\mathrm{CZ}}}, \tag{4}$$

which is related to the oft-studied Richardson number. In our evolved simulation, we measure $\mathcal{S} \sim 10^4$. Boundaries with a low stiffness $\mathcal{S} \lesssim 10$ easily deform in the presence of convective flows, but convective boundaries in stars often have $\mathcal{S} \gtrsim 10^6$. The number of convective overturn times required to entrain the SZ scale with $\mathcal{S}$; we have chosen to use a large value of $\mathcal{S}$ here to en-

---

[1] We ran simulations where N^2 was identical in the RZ and SZ and saw similar behavior. We make N^2 large in the RZ to reduce overshoot and wave mixing in the evolved state.
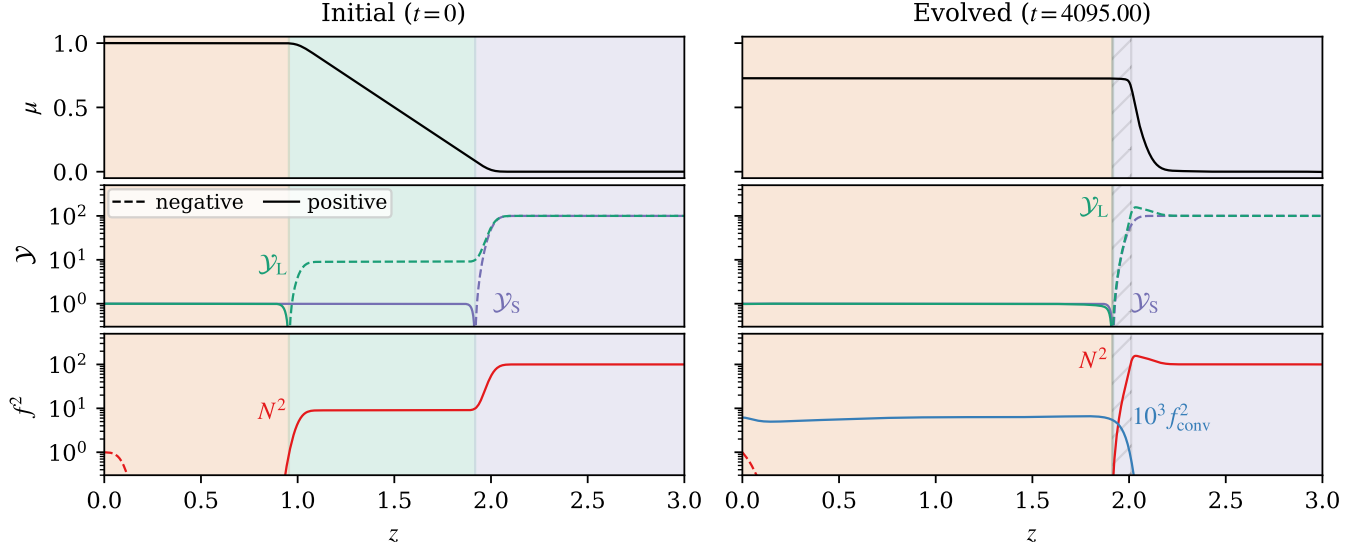
Figure 2. Horizontally-averaged profiles are shown for the composition (top), the discriminants $\mathcal{Y}_S$ and $\mathcal{Y}_L$ (middle, Eqns. 1 & 2), and the Brunt-Väisälä frequency $N^2 = -\mathcal{Y}_L$ and the square convective frequency f_{conv}^2 (bottom, Eqn. 3). Positive and negative values are respectively solid and dashed lines. We show the initial (left) and evolved (right, time-averaged over 100 convective overturn times) states. Note that there are no motions in the initial state, so $f_{conv}^2 = 0$ and does not appear. The background color is orange in CZs, green in SZs, and purple in RZs per Section 2. The lightly hashed background region in the evolved RZ is the mechanical overshoot zone. Note: this data is taken from a less turbulent run than fig 1; it'll be updated when the fig 1 run finishes.

₁₉₇ sure our simulations are in the right regime to study en-
₁₉₈ trainment at a stellar convective boundary. We briefly
₁₉₉ note that the entrainment timescale for the SZ scales like
₂₀₀ $\mathcal{S}^\alpha \tau_{dyn}$, where α is an $\mathcal{O}(1)$ positive exponent and τ_{dyn}
₂₀₁ is the dynamical timescale. Since the relevant timescale
₂₀₂ of evolution on the main sequence is the nuclear time
₂₀₃ τ_{nuc}, and since $\tau_{nuc}/\tau_{dyn} \gg \mathcal{S}^\alpha$ even for $\mathcal{S} \sim 10^6$, we ex-
₂₀₄ pect CZs to entrain SZs during a single stellar evolution
₂₀₅ time step.

₂₀₆   Finally, Figure 3 displays a Kippenhahn-like diagram
₂₀₇ of the simulation's height vs. time to show evolutionary
₂₀₈ trends. The roots of $\mathcal{Y}_L$ and $\mathcal{Y}_S$ are respectively shown
₂₀₉ as orange (Ledoux boundary) and purple (Schwarzschild
₂₁₀ boundary) lines. The CZ is colored orange and sits be-
₂₁₁ low the Ledoux boundary, the RZ is colored purple and
₂₁₂ sits above the Schwarzschild boundary, and the SZ is
₂₁₃ colored green and is between these boundaries. Con-
₂₁₄ vection motions overshoot above the Ledoux boundary.
₂₁₅ The height where the horizontally-averaged kinetic en-
₂₁₆ ergy falls below 10% of its bulk-CZ value is marked
₂₁₇ with a black line, and the hashed region below it is
₂₁₈ the overshoot zone. We note that the black line and
₂₁₉ overshoot zone roughly correspond with the maximum
₂₂₀ of $\partial\mu/\partial z$ (Fig. 2, upper right), so this describes over-
₂₂₁ shoot well. Importantly, note that the Schwarzschild
₂₂₂ and Ledoux boundaries start at different heights, but
₂₂₃ 3D convective mixing causes them to converge on dy-
₂₂₄ namical timescales.
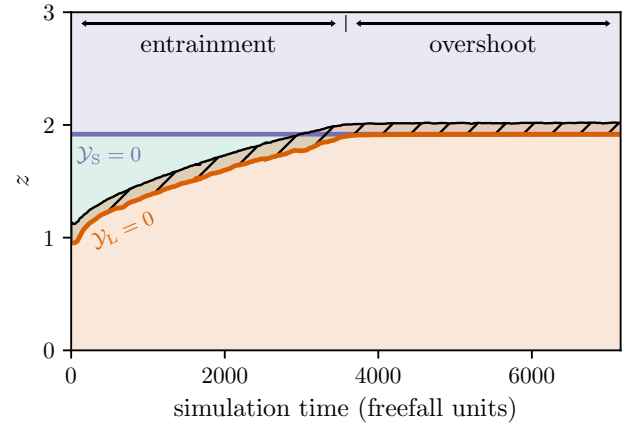
₂₂₅

Figure 3. A Kippenhahn-like diagram of the simulation evolution. The y-axis is simulation height and the x-axis is simulation time. The orange line denotes the Ledoux boundary ($\mathcal{Y}_L = 0$); the CZ is below this and is colored orange. The purple line denotes the Schwarzschild boundary ($\mathcal{Y}_S = 0$); the RZ is above this and is colored purple. The semiconvective region between these boundaries is colored green. The overshoot zone is hashed, and the black line denotes the top of this region. The simulation has an "entrainment phase" while the CZ expands, and a pure "overshoot phase" where the convective boundary does not advance. Note: this data is taken from a less turbulent run than fig 1; it'll be updated when the fig 1 run finishes.

4. CONCLUSIONS & DISCUSSION

In this letter, we presented a 3D simulation of a convection zone and its boundary. The convective boundary was initially compositionally stable but weakly thermally unstable (Ledoux stable but Schwarzschild unstable). Entrainment caused the convective boundary to advance until the boundary was stable by both the Schwarzschild and Ledoux criteria.

This simulation demonstrates that the Ledoux criterion *instantaneously* describes the location of a convective boundary. However, when the dynamical convective overturn timescale is short compared to the evolutionary timescale $t_{\rm evol} \gg \mathcal{S}^\alpha t_{\rm dyn}$ (see Sec. 3), the statistically-stationary location of the convective boundary will coincide with the Schwarzschild boundary. These 3D dynamics support the claim that "logically consistent" implementations of mixing length theory (Gabriel et al. 2014; Paxton et al. 2018, 2019) should have convective boundaries which are Schwarzschild-stable. Modern algorithms like the MESA software instrument's "convective pre-mixing" (CPM, Paxton et al. 2019) should agree with our results. The results of 1D stellar evolution calculations should not depend on the choice of stability criterion used when $t_{\rm evol} \gg \mathcal{S}^\alpha t_{\rm dyn}$.

We note briefly that many SZs (the middle layer of our simulations) in stars are unstable to oscillatory doubly-diffusive convection (ODDC). ODDC mixes composition gradients even more rapidly than the entrainment studied here, and has been studied extensively in local simulations (Mirouh et al. 2012; Wood et al. 2013; Xie et al. 2017); see the review of Garaud (2018). Moore & Garaud (2016) apply ODDC to the regions outside core convection zones in main sequence stars, and their results suggest that ODDC formulations should be widely included in stellar models.

For stages in stellar evolution where $\mathcal{S}^\alpha t_{\rm dyn} \sim t_{\rm evol}$, implementations of time-dependent convection (TDC, Kuhfuss 1986) should be employed to properly capture convective dynamics and the advancement of convective boundaries. The advancement of convective boundaries by e.g., entrainment in TDC implementations should be informed by time-dependent theories and simulations (e.g., Turner 1968; Fuentes & Cumming 2020).

The purpose of this study was to understand how the Ledoux boundary location evolves over time, and whether it coincides with the Schwarzschild boundary at late times. A detailed examination of convective overshoot is beyond the scope of this work (but see e.g., Korre et al. 2019). We furthermore constructed the simulations in this work to have negligible convective penetration per Anders et al. (2021). Finally, in stars, $\nabla_{\rm rad}$ and the Schwarzschild boundary location depend upon μ, but we made the assumption that the radiative conductivity and $\nabla_{\rm rad}$ do not depend on μ for simplicity. The nonlinear feedback between these effects should be studied in future work, but we do not expect that the fundamental takeaways of this work should change.

In summary, we find that the Ledoux criterion provides the instantaneous location of the convective boundary, and the Schwarzschild criterion provides the location of the convective boundary in a statistically stationary state; in this final state, the Ledoux and Schwarzschild criteria agree.

APPENDIX

A. MODEL & INITIAL CONDITIONS

In this work we study the simplest possible system: incompressible, Boussinesq convection with a composition field. These equations are

$$\boldsymbol{\nabla} \cdot \boldsymbol{u} = 0 \tag{A1}$$

$$\partial_t \boldsymbol{u} + \boldsymbol{u} \cdot \boldsymbol{\nabla} \boldsymbol{u} + \boldsymbol{\nabla}\varpi = \left(T - \frac{\mu}{\mathrm{R}_0}\right)\hat{z} + \frac{\mathrm{Pr}}{\mathrm{Pe}}\boldsymbol{\nabla}^2\boldsymbol{u}, \tag{A2}$$

$$\partial_t T + \boldsymbol{u} \cdot (\boldsymbol{\nabla}T - \hat{z}\,\partial_z T_{\rm ad}) + \boldsymbol{\nabla}\cdot[-\kappa_{T,0}\boldsymbol{\nabla}\overline{T}] = \frac{1}{\mathrm{Pe}}\boldsymbol{\nabla}^2 T', \tag{A3}$$

$$\partial_t \mu + \boldsymbol{u} \cdot \boldsymbol{\nabla}\mu = -\frac{\tau_0}{\mathrm{Pe}}\boldsymbol{\nabla}^2\overline{\mu} + \frac{\tau}{\mathrm{Pe}}\boldsymbol{\nabla}^2\mu'. \tag{A4}$$

Here, $\boldsymbol{u}$ is velocity, T is temperature, and μ is concentration. Bars (e.g., $\overline{T}$) represent the horizontally-averaged component of a field and primes (e.g., T') denote all fluctuations around that background. The adiabatic temperature gradient is $\partial_z T_{\mathrm{ad}}$ and the nondimensional control parameters are

$$
\mathrm{Pe} = \frac{\mathrm{u_{ff}}\ell_{\mathrm{conv}}}{\kappa_{\mathrm{T}}}, \qquad \mathrm{R}_0 = \frac{|\alpha|\Delta\mathrm{T}}{|\beta|\Delta\mu},
$$
$$
\mathrm{Pr} = \frac{\nu}{\kappa_T}, \qquad \tau = \frac{\kappa_\mu}{\kappa_T}, \tag{A5}
$$

where the nondimensional freefall velocity is $\boldsymbol{u}_{\mathrm{ff}} = \sqrt{|\alpha|g\ell_{\mathrm{conv}}\Delta T}$ (with gravitational acceleration g), ℓ_{conv} is the initial depth of the convection zone, $\Delta\mu$ is the composition change across the Ledoux stable region, $\Delta T = \ell_{\mathrm{conv}}(\partial_z T_{\mathrm{rad}} - \partial_z T_{\mathrm{ad}})$ is the superadiabatic temperature scale of the convection zone, α and β are the coefficients of expansion for T and μ, ν is the viscosity, κ_T is the thermal diffusivity, and κ_μ is the compositional diffusivity. Eqns. A1-A4 are identical to Eqns. 2-5 in Garaud (2018), except we modify the diffusion coefficients acting on $\overline{T}$ ($\kappa_{T,0}$) and $\overline{\mu}$ (τ_0). By doing this, the radiative temperature gradient $\partial_z T_{\mathrm{rad}} = -\mathrm{Flux}/\kappa_{T,0}$ can change with height, and we reduce diffusion on $\overline{\mu}$ to ensure its evolution is due to advection.

We define the Ledoux and Schwarzschild discriminants

$$
\mathcal{Y}_{\mathrm{S}} = \left(\frac{\partial T}{\partial z}\right)_{\mathrm{rad}} - \left(\frac{\partial T}{\partial z}\right)_{\mathrm{ad}}, \quad \mathcal{Y}_{\mathrm{L}} = \mathcal{Y}_{\mathrm{S}} - \mathrm{R}_0^{-1}\frac{\partial\mu}{\partial z}, \tag{A6}
$$

and in this nondimensional system the Brunt-Väisälä frequency is the negative of the Ledoux discriminant $N^2 = -\mathcal{Y}_{\mathrm{L}}$.

In this work, we study a three-layer model in $z = [0, 3]$,

$$
\left(\frac{\partial T}{\partial z}\right)_{\mathrm{rad}} = \left(\frac{\partial T}{\partial z}\right)_{\mathrm{ad}} + \begin{cases} -1 & z \le 2 \\ 10\mathrm{R}_0^{-1} & z > 2 \end{cases}, \tag{A7}
$$

$$
\frac{\partial\mu_0}{\partial z} = \begin{cases} 0 & z \le 1 \\ -1 & 1 < z \le 2 \\ 0 & 2 < z \end{cases}, \tag{A8}
$$

We set $\mu = 1$ at $z = 0$ and $T = 1$ at $z = 3$. The the intial temperature profile has $\partial_z T_0 = \partial_z T_{\mathrm{rad}}$ everywhere except between $z = [0.1, 1]$ where $\partial_z T_0 = \partial_z T_{\mathrm{ad}}$. We set $(\partial T/\partial z)_{\mathrm{ad}} = -1 - 10\mathrm{R}_0^{-1}$.

B. SIMULATION DETAILS & DATA AVAILABILITY

We time-evolve equations A1-A4 using the Dedalus pseudospectral solver (Burns et al. 2020, git commit 1339061) using timestepper SBDF2 (Wang & Ruuth 2008) and safety factor 0.3. All variables are spectral expansions of Chebyshev coefficients in the vertical (z) direction ($n_z = 512$ between $z = [0, 2.25]$ plus $n_z = 64$ between $z = [2.25, 3]$) and as $(n_x, n_y) = (192, 192)$ Fourier coefficients in the horizontally periodic (x, y) directions. Our domain spans $x \in [0, L_x]$, $y \in [0, L_y]$, and $z \in [0, L_z]$ with $L_x = L_y = 4$ and $L_z = 3$. To avoid aliasing errors, we use the 3/2-dealiasing rule in all directions. To start our simulations, we add random noise temperature perturbations with a magnitude of 10^{-6} to the initial temperature profile.

Spectral methods with finite coefficient expansions cannot capture true discontinuities. To approximate discontinuous functions such as Eqns. A7 & A8, we define a smooth Heaviside step function centered at $z = z_0$,

$$
H(z; z_0, d_w) = \frac{1}{2}\left(1 + \mathrm{erf}\left[\frac{z - z_0}{d_w}\right]\right). \tag{B9}
$$

where erf is the error function and we set $d_w = 0.05$. The simulation in this work uses $\mathcal{P} = 3.2 \times 10^3$, $\mathrm{R}_0^{-1} = 10$, $\mathrm{Pr} = \tau = 0.5$, $\tau_0 = 1.5 \times 10^{-3}$, and $\kappa_{T,0} = \mathcal{P}^{-1}[(\partial T/\partial z)_{\mathrm{rad}}|_{z=0}]/(\partial T/\partial z)_{\mathrm{rad}}$

We produce figures 2 and 3 using matplotlib (Hunter 2007; Caswell et al. 2021). We produce figure 1 using plotly (Inc. 2015) and matplotlib. All of the Python scripts used to run the simulations in this paper and to create the figures in this paper are publicly available in a git repository (https://github.com/evanhanders/schwarzschild_or_ledoux) and in a Zenodo repository (**?**).

REFERENCES

Anders, E. H., Jermyn, A. S., Lecoanet, D., & Brown, B. P. 2021, arXiv e-prints, arXiv:2110.11356. https://arxiv.org/abs/2110.11356

Andrassy, R., Herwig, F., Woodward, P., & Ritter, C. 2020, MNRAS, 491, 972, doi: 10.1093/mnras/stz2952

Andrassy, R., Higl, J., Mao, H., et al. 2021, arXiv e-prints, arXiv:2111.01165. https://arxiv.org/abs/2111.01165

Basu, S. 2016, Living Reviews in Solar Physics, 13, 2, doi: 10.1007/s41116-016-0003-4

Basu, S., Verner, G. A., Chaplin, W. J., & Elsworth, Y. 2012, ApJ, 746, 76, doi: 10.1088/0004-637X/746/1/76

Burns, K. J., Vasil, G. M., Oishi, J. S., Lecoanet, D., & Brown, B. P. 2020, Physical Review Research, 2, 023068, doi: 10.1103/PhysRevResearch.2.023068

Carlos, M., Meléndez, J., Spina, L., et al. 2019, MNRAS, 485, 4052, doi: 10.1093/mnras/stz681

Caswell, T. A., Droettboom, M., Lee, A., et al. 2021, matplotlib/matplotlib: REL: v3.3.4, v3.3.4, Zenodo, doi: 10.5281/zenodo.4475376

Claret, A., & Torres, G. 2018, ApJ, 859, 100, doi: 10.3847/1538-4357/aabd35

Cristini, A., Hirschi, R., Meakin, C., et al. 2019, MNRAS, 484, 4645, doi: 10.1093/mnras/stz312

Dumont, T., Palacios, A., Charbonnel, C., et al. 2021, A&A, 646, A48, doi: 10.1051/0004-6361/202039515

Farmer, R., Renzo, M., de Mink, S. E., Marchant, P., & Justham, S. 2019, ApJ, 887, 53, doi: 10.3847/1538-4357/ab518b

Fuentes, J. R., & Cumming, A. 2020, Physical Review Fluids, 5, 124501, doi: 10.1103/PhysRevFluids.5.124501

Gabriel, M., Noels, A., Montalbán, J., & Miglio, A. 2014, A&A, 569, A63, doi: 10.1051/0004-6361/201423442

Garaud, P. 2018, Annual Review of Fluid Mechanics, 50, 275, doi: 10.1146/annurev-fluid-122316-045234

Georgy, C., Saio, H., & Meynet, G. 2021, A&A, 650, A128, doi: 10.1051/0004-6361/202040105

Hunter, J. D. 2007, Computing in Science and Engineering, 9, 90, doi: 10.1109/MCSE.2007.55

Inc., P. T. 2015, Collaborative data science, Montreal, QC: Plotly Technologies Inc. https://plot.ly

Johnston, C. 2021, A&A, 655, A29, doi: 10.1051/0004-6361/202141080

Jones, S., Andrassy, R., Sandalski, S., et al. 2017, MNRAS, 465, 2991, doi: 10.1093/mnras/stw2783

Kaiser, E. A., Hirschi, R., Arnett, W. D., et al. 2020, MNRAS, 496, 1967, doi: 10.1093/mnras/staa1595

Korre, L., Garaud, P., & Brummell, N. H. 2019, MNRAS, 484, 1220, doi: 10.1093/mnras/stz047

Kuhfuss, R. 1986, A&A, 160, 116

Meakin, C. A., & Arnett, D. 2007, ApJ, 667, 448, doi: 10.1086/520318

Mehta, A. K., Buonanno, A., Gair, J., et al. 2022, ApJ, 924, 39, doi: 10.3847/1538-4357/ac3130

Mirouh, G. M., Garaud, P., Stellmach, S., Traxler, A. L., & Wood, T. S. 2012, ApJ, 750, 61, doi: 10.1088/0004-637X/750/1/61

Moore, K., & Garaud, P. 2016, ApJ, 817, 54, doi: 10.3847/0004-637X/817/1/54

Morrell, S. A. F. 2020, PhD thesis, University of Exeter

Paxton, B., Schwab, J., Bauer, E. B., et al. 2018, ApJS, 234, 34, doi: 10.3847/1538-4365/aaa5a8

Paxton, B., Smolec, R., Schwab, J., et al. 2019, ApJS, 243, 10, doi: 10.3847/1538-4365/ab2241

Pedersen, M. G., Aerts, C., Pápics, P. I., et al. 2021, arXiv e-prints, arXiv:2105.04533. https://arxiv.org/abs/2105.04533

Pinsonneault, M. 1997, ARA&A, 35, 557, doi: 10.1146/annurev.astro.35.1.557

Salaris, M., & Cassisi, S. 2017, Royal Society Open Science, 4, 170192, doi: 10.1098/rsos.170192

Scott, L. J. A., Hirschi, R., Georgy, C., et al. 2021, MNRAS, 503, 4208, doi: 10.1093/mnras/stab752

Sestito, P., & Randich, S. 2005, A&A, 442, 615, doi: 10.1051/0004-6361:20053482

Staritsin, E. I. 2013, Astronomy Reports, 57, 380, doi: 10.1134/S1063772913050089

Turner, J. S. 1968, Journal of Fluid Mechanics, 33, 183, doi: 10.1017/S0022112068002442

Viani, L. S., & Basu, S. 2020, ApJ, 904, 22, doi: 10.3847/1538-4357/abba17

Wang, D., & Ruuth, S. J. 2008, Journal of Computational Mathematics, 26, 838. http://www.jstor.org/stable/43693484

Wood, T. S., Garaud, P., & Stellmach, S. 2013, ApJ, 768, 157, doi: 10.1088/0004-637X/768/2/157

Woodward, P. R., Herwig, F., & Lin, P.-H. 2015, ApJ, 798, 49, doi: 10.1088/0004-637X/798/1/49

Xie, J.-H., Miquel, B., Julien, K., & Knobloch, E. 2017, Fluids, 2, doi: 10.3390/fluids2010006